A Few Benchmark Test Cases for Higher-Order Euler Solvers

Liang Pan[1], Jiequan Li[1,*], Kun Xu[2,3]

[1]*Laboratory of Computational Physics, Institute of Applied Physics and Computational Mathematics, Beijing, China*
[2]*Department of Mathematics, Hong Kong University of Science and Technology, Clear Water Bay, Kowloon, Hong Kong*
[3]*Department of Mechanical and Aerospace Engineering, Hong Kong University of Science and Technology, Clear Water Bay, Kowloon, Hong Kong*

Abstract. There have been great efforts on the development of higher-order numerical schemes for compressible Euler equations in recent decades. The traditional test cases proposed thirty years ago mostly target on the strong shock interactions, which may not be adequate enough for evaluating the performance of current higher-order schemes. In order to set up a higher standard for the development of new algorithms, in this paper we present a few benchmark cases with severe and complicated wave structures and interactions, which can be used to clearly distinguish different kinds of higher-order schemes. All tests are selected so that the numerical settings are very simple and any higher order scheme can be straightforwardly applied to these cases. The examples include highly oscillatory solutions and the large density ratio problem in one dimensional case. In two dimensions, the cases include hurricane-like solutions; interactions of planar contact discontinuities with asymptotic large Mach number (the composite of entropy wave and vortex sheets); interaction of planar rarefaction waves with transition from continuous flows to the presence of shocks; and other types of interactions of two-dimensional planar waves. To get good performance on all these cases may push algorithm developer to seek for new methodology in the design of higher-order schemes, and improve the robustness and accuracy of higher-order schemes to a new level of standard. In order to give reference solutions, the fourth-order gas-kinetic scheme (GKS) will be used to all these benchmark cases, even though the GKS solutions may not be very accurate in some cases. The main purpose of this paper is to recommend other CFD researchers to try these cases as well, and promote further development of higher-order schemes.

Corresponding author. Email addresses: `panliangjlu@sina.com` (L. Pan), `li_jiequan@iapcm.ac.cn` (J. Q. Li), `makxu@ust.hk` (K. Xu)

1. Introduction

In past decades, there have been tremendous efforts on designing high-order accurate numerical schemes for compressible flows and great success has been achieved. The developments of high-order accurate numerical schemes were pioneered by Lax and Wendroff [22], and extended into the version of high resolution methods by Kolgan [18], Boris [7], van Leer [44], Harten [13] et al, and other higher order versions, such as Essentially Non-Oscillatory (ENO) [16, 41], Weighted Essentially Non-Oscillatory (WENO) [17, 31], Discontinuous Galerkin (DG) [10, 12, 35] methods etc.

In the past decades, the evaluation of the performance of numerical scheme was mostly based on the test cases with strong shocks for capturing sharp shock transition, such as the blast wave interaction, the forward step-facing flows, and the double Mach reflection [45]. Now it is not a problem at all for shock capturing scheme to get stable sharp shock transition. However, with the further development of higher order numerical methods and practical demands (such as turbulent flow simulations), more challenging test problems for capturing multiple wave structure are expected to be used. For testing higher-order schemes, the setting of these cases should be sufficiently simple and easy for coding, and avoid the possible pollution from the boundary condition and curvilinear meshes. To introduce a few tests which can be truthfully used to evaluate the performance of higher-order scheme is the motivation of the current paper. Our selected examples include the following ones: one-dimensional cases, two-dimensional Riemann problems, and the conservation law with source terms. For the one-dimensional problems, the first case is a highly oscillatory shock-turbulence interaction problem, which is an extension of Shu-Osher problem by Titarev and Toro [43] with much more severe oscillations, and the second one is a large density ratio problem with a very strong rarefaction wave in the solution [42], which can be used to test the robustness and accuracy in capturing strong expansion waves. For the two-dimensional cases, four group wave interactions are tested. (i) Hurricane-like solutions [27, 48], which are highly nontrivial two-dimensional time-dependent solutions with one-point vacuum in the center and rotational velocity field. It is proposed to test the preservation of positivity and symmetry of the numerical scheme. (ii) The interaction of planar contact discontinuities for different Mach numbers. The multidimensional contact discontinuities are the composite of entropy waves and vortex sheets. The simulation of these cases is associated with difficulties for capturing the strong shear effects. Since at the large Mach number limits these cases have explicit solutions [27, 40], they are proposed here to check the ability of higher-order schemes in capturing wave structures of various scales and the asymptotic property. (iii) Interaction of planar rarefaction waves with the transition from continuous fluid flows to the presence of shocks. (iv) Further interaction of planar shocks with Mach reflection phenomenon. These two-dimensional problems fall into the category of two-dimensional Riemann problems proposed in [49]. The two-dimensional Riemann problems reveal almost all substantial wave patterns of shock reflections, spiral formations, vortex-shock interactions, and so on, through simple classification of initial data. The rich wave configurations conjectured in [49] have been confirmed numerically by several subsequent works [14, 20, 27, 37]. Since the formula-

tions of these problems are extremely simple, without complicated numerical boundary treatment, they are suitable as benchmark tests. The case for the conservation law with source term is also proposed.

In order to provide reference solutions for all these test cases. A gas-kinetic scheme will be used to calculate the solutions in this paper. Recently, based on the time-dependent flux function of the generalized Riemann problem (GRP) solver [3–5], a two-stage fourth-order time-accurate discretization was developed for Lax-Wendroff type flow solvers, particularly applied for the hyperbolic conservation laws [26]. The reason for the success of a two-stage L-W type time stepping method in achieving a fourth-order temporal accuracy is solely due to the use of both flux function and its temporal derivative. In terms of the gas evolution model, the gas-kinetic scheme provides a temporal accurate flux function as well, even though it depends on time through a much more complicated relaxation process from the kinetic to the hydrodynamic scale physics than the time-dependent flux function of GRP. Based on this time-stepping method and the second-order gas-kinetic solver [46, 47], a fourth-order gas-kinetic scheme was constructed for the Euler and Navier-Stokes equations [34]. In comparison with the formal one-stage time-stepping third-order gas-kinetic solver [30,32], the fourth-order scheme not only reduces the complexity of the flux function, but also improves the accuracy of the scheme, even though the third-order and fourth-order schemes take similar computation cost. The robustness of the fourth-order gas-kinetic scheme is as good as the second-order one. Numerical tests show that the fourth-order scheme not only has the expected order of accuracy for the smooth flows, but also has favorable shock capturing property for the discontinuous solutions. The fourth-order GKS will not definitely provide the most accurate solutions for all these tests. The reason for choosing GKS is that this scheme can at least provide reasonable solutions whenever the analytic or asymptotic results are available. Many existing higher-order schemes may have difficulties to pass all these cases and provide accurate solutions, especially for the schemes with over-simplified flux function [42].

This paper is organized as follows. In Section 2, we will briefly review the fourth-order gas-kinetic scheme. In Section 3, we present the benchmark test cases and provide the GKS reference solutions. The final conclusion is made in the last section.

2. The review of two-stage fourth-order gas-kinetic scheme

In this section, we will briefly review our recently developed two-stage fourth-order gas-kinetic scheme. This scheme is developed in the framework of finite volume scheme, and it contains three standard ingredients: spatial data reconstruction, two-stage time stepping discretization, and second-order gas-kinetic flux function.

2.1. Spatial reconstruction

The spatial reconstruction for the gas-kinetic scheme contains two parts, i.e., initial data reconstruction and reconstruction for equilibrium. In this paper, the fifth-order WENO method [17] is used for the initial data reconstruction. Assume that W are the macroscopic

flow variables that need to be reconstructed. W_i are the cell averaged values, and W_i^r, W_i^l are the two values obtained by the reconstruction at two ends of the i-th cell. The fifth-order WENO reconstruction is given as follows

$$W_i^r = \sum_{k=0}^{2} w_k w_k^r, \qquad W_i^l = \sum_{k=0}^{2} \widetilde{w}_k w_k^l,$$

where all quantities involved are taken as

$$w_0^r = \frac{1}{3}W_i + \frac{5}{6}W_{i+1} - \frac{1}{6}W_{i+2}, \qquad w_0^l = \frac{11}{6}W_i - \frac{7}{6}W_{i+1} + \frac{1}{3}W_{i+2},$$

$$w_1^r = -\frac{1}{6}W_{i-1} + \frac{5}{6}W_i + \frac{1}{3}W_{i+1}, \qquad w_1^l = \frac{1}{3}W_{i-1} + \frac{5}{6}W_i - \frac{1}{6}W_{i+1},$$

$$w_2^r = \frac{1}{3}W_{i-2} - \frac{7}{6}W_{i-1} + \frac{11}{6}W_i, \qquad w_2^l = -\frac{1}{6}W_{i-2} + \frac{5}{6}W_{i-1} + \frac{1}{3}W_i,$$

and w_k, $\widetilde{w}_k$, $k = 0, 1, 2$ are the nonlinear weights. The most widely used is the WENO-JS non-linear weights [17], which can be written as follows

$$w_k^{JS} = \frac{\alpha_k^{JS}}{\sum_{p=0}^{2} \alpha_p^{JS}}, \quad \alpha_k^{JS} = \frac{d_k}{(\epsilon + \beta_k)^2}, \quad \widetilde{w}_k^{JS} = \frac{\widetilde{\alpha}_s^{JS}}{\sum_{p=0}^{2} \widetilde{\alpha}_p^{JS}}, \quad \widetilde{\alpha}_k^{JS} = \frac{\widetilde{d}_k}{(\epsilon + \beta_k)^2},$$

where

$$d_0 = \widetilde{d}_2 = \frac{3}{10}, \quad d_1 = \widetilde{d}_1 = \frac{3}{5}, \quad d_2 = \widetilde{d}_0 = \frac{1}{10}, \quad \epsilon = 10^{-6},$$

and β_k is the smooth indicator, and the basic idea for its construction can be found in [31]. In order to achieve a better performance of the WENO scheme near smooth extrema, WENO-Z [1] and WENO-Z+ [2] reconstruction were developed. The only difference is the nonlinear weights. The nonlinear weights for the WENO-Z method is written as

$$w_k^Z = \frac{\alpha_k^Z}{\sum_{k=0}^{2} \alpha_k^Z}, \qquad \alpha_k^Z = d_k \left[1 + \left(\frac{\delta}{\epsilon + \beta_k} \right)^2 \right],$$

and the nonlinear weights for the WENO-Z+ method is

$$w_k^{Z+} = \frac{\alpha_k^{Z+}}{\sum_{k=0}^{2} \alpha_k^{Z+}}, \qquad \alpha_k^{Z+} = d_k \left[1 + \left(\frac{\delta + \epsilon}{\epsilon + \beta_k} \right)^2 + \lambda \left(\frac{\epsilon + \beta_k}{\delta + \epsilon} \right) \right],$$

where β_k is the same local smooth indicator as in [17], $\delta = |\beta_0 - \beta_2|$ is used for the fifth-order reconstruction, and λ is a parameter for fine-tuning the size of the weight of less smooth stencils. In the numerical tests, without special statement, WENO-JS method will be used for initial data reconstruction.

After the initial date reconstruction, the reconstruction of equilibrium part is presented. For the cell interface $x_{i+1/2}$, the reconstructed variables at both sides of the cell interface

are denoted as W_l, W_r. According to the compatibility condition, which will be given later, the macroscopic variables at the cell interface is obtained and denoted as W_0. The conservative variables around the cell interface can be expanded as

$$\overline{W}(x) = W_0 + S_1(x - x_*) + \frac{1}{2}S_2(x - x_*)^2 + \frac{1}{6}S_3(x - x_*)^3 + \frac{1}{24}S_4(x - x_*)^4.$$

With the following conditions,

$$\int_{I_{i+k}} \overline{W}(x) = W_{i+k}, \quad k = -1, \cdots, 2,$$

the derivatives are given by

$$\overline{W}_x = S_1 = \frac{1}{\Delta x}\left[-\frac{1}{12}(W_{i+2} - W_{i-1}) + \frac{5}{4}(W_{i+1} - W_i)\right].$$

2.2. Two-stage fourth-order temporal discretization

The two-stage fourth-order temporal discretization was developed for Lax-Wendroff flow solvers, and was originally applied for the generalized Riemann problem solver (GRP) [26] for hyperbolic equations. In [9, 38], multi-stage multi-derivative time stepping methods were proposed and developed as well under different framework of flux evaluation. Consider the following time-dependent equation

$$\frac{\partial \mathbf{w}}{\partial t} = \mathscr{L}(\mathbf{w}), \tag{2.1}$$

with the initial condition at t_n, i.e.,

$$\mathbf{w}(t = t_n) = \mathbf{w}^n, \tag{2.2}$$

where $\mathscr{L}$ is an operator for spatial derivative of flux. The time derivatives are obtained using the Cauchy-Kovalevskaya method,

$$\frac{\partial \mathbf{w}^n}{\partial t} = \mathscr{L}(\mathbf{w}^n), \qquad \frac{\partial}{\partial t}\mathscr{L}(\mathbf{w}^n) = \frac{\partial}{\partial \mathbf{w}}\mathscr{L}(\mathbf{w}^n)\mathscr{L}(\mathbf{w}^n).$$

Introducing an intermediate state at $t^* = t_n + \Delta t/2$,

$$\mathbf{w}^* = \mathbf{w}^n + \frac{1}{2}\Delta t \mathscr{L}(\mathbf{w}^n) + \frac{1}{8}\Delta t^2 \frac{\partial}{\partial t}\mathscr{L}(\mathbf{w}^n), \tag{2.3}$$

the corresponding time derivatives are obtained as well for the intermediate stage state,

$$\frac{\partial \mathbf{w}^*}{\partial t} = \mathscr{L}(\mathbf{w}^*), \qquad \frac{\partial}{\partial t}\mathscr{L}(\mathbf{w}^*) = \frac{\partial}{\partial \mathbf{w}}\mathscr{L}(\mathbf{w}^*) \cdot \mathscr{L}(\mathbf{w}^*).$$

Then, a fourth-order temporal accuracy solution of $\mathbf{w}(t)$ at $t = t_n + \Delta t$ can be provided by the following equation

$$\mathbf{w}^{n+1} = \mathbf{w}^n + \Delta t \mathscr{L}(\mathbf{w}^n) + \frac{1}{6}\Delta t^2 \left(\frac{\partial}{\partial t}\mathscr{L}(\mathbf{w}^n) + 2\frac{\partial}{\partial t}\mathscr{L}(\mathbf{w}^*) \right). \tag{2.4}$$

The details of this analysis can be found in [26]. Thus, a fourth-order temporal accuracy can be achieved by the two-stage discretization Eq. (2.3) and Eq. (2.4).

Consider the following conservation laws

$$\frac{\partial \mathbf{w}}{\partial t} + \frac{\partial \mathbf{f}(\mathbf{w})}{\partial x} = 0.$$

The semi-discrete form of a finite volume scheme can be written as

$$\frac{\partial \mathbf{w}_i}{\partial t} = \mathscr{L}_i(\mathbf{w}) = -\frac{1}{\Delta x}(\mathbf{f}_{i+1/2} - \mathbf{f}_{i-1/2}),$$

where $\mathbf{w}_i$ are the cell averaged conservative variables, $\mathbf{f}_{i+1/2}$ are the fluxes at the cell interface $x = x_{i+1/2}$, and Δx is the cell size. With the temporal derivatives of the flux, the two-stage fourth-order scheme can be developed [26, 34]. Similarly, for the conservation laws with source terms

$$\frac{\partial \mathbf{w}}{\partial t} + \frac{\partial \mathbf{f}(\mathbf{w})}{\partial x} = S(\mathbf{w}),$$

the corresponding operator can be denoted as

$$\mathscr{L}_i(\mathbf{w}) = -\frac{1}{\Delta x}(\mathbf{f}_{i+1/2} - \mathbf{f}_{i-1/2}) + S(\mathbf{w}_i). \tag{2.5}$$

The two-stage fourth-order temporal discretization can be directly extended for conservation laws with source terms.

2.3. Second-order gas-kinetic flux solver

The two-dimensional BGK equation [6, 8] can be written as

$$f_t + \mathbf{u} \cdot \nabla f = \frac{g - f}{\tau}, \tag{2.6}$$

where f is the gas distribution function, g is the corresponding equilibrium state, and τ is the collision time. The collision term satisfies the compatibility condition

$$\int \frac{g - f}{\tau} \psi d\Xi = 0, \tag{2.7}$$

where $\psi = \left(1, \ u, \ v, \ \frac{1}{2}(u^2 + v^2 + \xi^2)\right)$, $d\Xi = du dv d\xi^1 \cdots d\xi^K$, K is number of internal freedom, i.e. $K = (4 - 2\gamma)/(\gamma - 1)$ for two-dimensional flows, and γ is the specific heat ratio.

To update the flow variables in the finite volume framework, the integral solution of BGK equation Eq. (2.6) is used to construct the gas distribution function at a cell interface, which can be written as

$$f(x_{i+1/2}, t, u, v, \xi)$$
$$= \frac{1}{\tau} \int_0^t g(x', y', t', u, v, \xi) e^{-(t-t')/\tau} dt' + e^{-t/\tau} f_0(-ut, y - vt, u, v, \xi), \qquad (2.8)$$

where $x_{i+1/2} = 0$ is the location of the cell interface, $x_{i+1/2} = x' + u(t - t')$ and $y = y' + v(t - t')$ are the trajectory of particles, f_0 is the initial gas distribution function, and g is the corresponding equilibrium state. The time dependent integral solution at the cell interface $x_{i+1/2}$ can be expressed as

$$f(x_{i+1/2}, t, u, v, \xi)$$
$$= (1 - e^{-t/\tau}) g_0 + \left((t + \tau) e^{-t/\tau} - \tau \right) \left(\overline{a}_1 u + \overline{a}_2 v \right) g_0 + (t - \tau + \tau e^{-t/\tau}) \overline{A} g_0$$
$$+ e^{-t/\tau} g_r [1 - (\tau + t)(a_{1r} u + a_{2r} v) - \tau A_r)] H(u)$$
$$+ e^{-t/\tau} g_l [1 - (\tau + t)(a_{1l} u + a_{2l} v) - \tau A_l)] (1 - H(u)). \qquad (2.9)$$

Based on the spatial reconstruction of macroscopic flow variables, which is presented before, the conservative variables W_l and W_r on the left and right hand sides of a cell interface, and the corresponding equilibrium states g_l and g_r, can be determined. The conservative variable W_0 and the equilibrium state g_0 at the cell interface can be determined according to the compatibility condition Eq. (2.7) as follows

$$\int \psi g_0 d\Xi = W_0 = \int_{u>0} \psi g_l d\Xi + \int_{u<0} \psi g_r d\Xi.$$

The coefficients related to the spatial derivatives and time derivative a_{1k}, a_{2k}, A_k, $k = l, r$ and $\overline{a}_1$, $\overline{a}_2$, $\overline{A}$ in gas distribution function Eq. (2.9) can be determined according to the spatial derivatives and compatibility condition. More details of the gas-kinetic scheme can be found in [46].

As mentioned in the section before, in order to utilize the two-stage temporal discretization, the temporal derivatives of the flux function need to be determined. While in order to obtain the temporal derivatives at t_n and $t_* = t_n + \Delta t/2$ with the correct physics, the flux function should be approximated as a linear function of time within the time interval. Let's first introduce the following notation,

$$\mathbb{F}_{i+1/2}(W^n, \delta) = \int_{t_n}^{t_n + \delta} F_{i+1/2}(W^n, t) dt = \int_{t_n}^{t_n + \delta} \int u \psi f(x_{i+1/2}, t, u, v, \xi) du d\xi dt.$$

In the time interval $[t_n, t_n + \Delta t]$, the flux is expanded as the following linear form

$$F_{i+1/2}(W^n, t) = F_{i+1/2}^n + \partial_t F_{i+1/2}^n (t - t_n). \qquad (2.10)$$

The coefficients $F_{j+1/2}^n$ and $\partial_t F_{j+1/2}^n$ can be fully determined as follows

$$F_{i+1/2}(W^n, t_n)\Delta t + \frac{1}{2}\partial_t F_{i+1/2}(W^n, t_n)\Delta t^2 = \mathbb{F}_{i+1/2}(W^n, \Delta t),$$

$$\frac{1}{2}F_{i+1/2}(W^n, t_n)\Delta t + \frac{1}{8}\partial_t F_{i+1/2}(W^n, t_n)\Delta t^2 = \mathbb{F}_{i+1/2}(W^n, \Delta t/2).$$

Similarly, $F_{i+1/2}(W^*, t_*)$, $\partial_t F_{i+1/2}(W^*, t_*)$ for the intermediate stage $t_n + \Delta t/2$ can be constructed as well.

Thus, we have completed the review of three building blocks of fourth-order gas-kinetic scheme, i.e., spatial data reconstruction, two-stage temporal discretization, and second-order gas-kinetic flux solver. More details about the implementation of the fourth-order gas-kinetic scheme can be found in [34].

3. Benchmark test cases

In this section, we present the benchmark test cases for the compressible Euler equations. The two-dimensional Euler equations are

$$\frac{\partial}{\partial t}\begin{pmatrix} \rho \\ \rho U \\ \rho V \\ \rho E \end{pmatrix} + \frac{\partial}{\partial x}\begin{pmatrix} \rho U \\ \rho U^2 + p \\ \rho UV \\ U(\rho E + p) \end{pmatrix} + \frac{\partial}{\partial y}\begin{pmatrix} \rho V \\ \rho UV \\ \rho V^2 + p \\ V(\rho E + p) \end{pmatrix} = 0, \tag{3.1}$$

where ρ is the density, U, V are velocity components, p is the pressure, and

$$\rho E = \frac{1}{2}\rho(U^2 + V^2) + \frac{p}{\gamma - 1}.$$

In the computation, the collision time τ in gas-kinetic scheme for the inviscid flows takes

$$\tau = \varepsilon\Delta t + C\left|\frac{p_l - p_r}{p_l + p_r}\right|\Delta t,$$

where $\varepsilon = 0.05$, $C = 1$, p_l and p_r denote the pressure on the left and right sides of the cell interface. The reason for including artificial dissipation through the additional term in the particle collision time is to enlarge the kinetic scale physics in the discontinuous region for the construction of a numerical shock structure through the particle free transport and inadequate particle collision for keeping the non-equilibrium property in the shock region. In all simulations, the Courant number $CFL = 0.4$. Without special statement, the specific heat ratio $\gamma = 1.4$.

In order to set up a new standard to guide the further development of higher-order schemes, in this paper we suggest a few benchmark cases in one- and two-dimensions for the compressible Euler solutions as well. The tested cases are listed as follows,

1. One-dimensional problems

    (a) Titarev-Toro's highly oscillatory shock-entropy wave interaction;

    (b) Large density ratio problem with a very strong rarefaction wave.

2. Two-dimensional Riemann problems

    (a) Hurrican-like solutions with one-point vacuum and rotational velocity field;

    (b) Interaction of planar contact discontinuities, with the involvement of entropy wave and vortex sheets;

    (c) Interaction of planar rarefaction waves with the transition from continuous flow to the presence of shock;

    (d) Interaction of planar (oblique) shocks.

3. Conservation law with source terms

    (a) Rayleigh-Taylor instability.

3.1. One-dimensional problems

The first one-dimensional problem is the extension of the Shu-Osher problem given by Titarev and Toro [43] to test a severely oscillatory wave interacting with shock. It aims to test the ability of high-order numerical scheme to capture the extremely high frequency waves. The initial condition for this case is given as follows,

$$(\rho, U, p) = \begin{cases} (1.515695, \ 0.523346, \ 1.805), & -5 < x \le -4.5, \\ (1 + 0.1\sin(20\pi x), \ 0, \ 1), & -4.5 < x < 5. \end{cases}$$

The computational domain is $[-5, 5]$ and 1000 uniform cells are used, and the density distributions at $t = 5$ are presented. WENO-JS, WENO-Z and WENO-Z+ methods are used to test the performance of different nonlinear weights in the WENO reconstruction. The density distribution and local enlargement of Titarev-Toro problem with different weights are given in Fig. 1, where $\lambda = \Delta x^{3/4}$ in WENO-Z+ methods. Similar to the results in [2], with a proper choice of the parameter λ, WENO-Z+ method performs much better than WENO-JS and WENO-Z methods. In order to check the role of λ in WENO-Z+ method, the density distributions are presented in Fig. 2, for the cases with $\lambda = \Delta x^{1/2}, \Delta x^{3/4}$ and Δx. It shows that the numerical performance is very sensitive to the choice of λ, which is also observed in [2]. However, the current scheme with GKS formulation tends to provide better results than those in [2] in all cases with $\lambda = \Delta x^{1/2}, \Delta x^{3/4}$ and Δx due to the self-adjusting (or time-dependent) dynamics in the GKS flux function.

The second example is the large density ratio problem with a very strong rarefaction wave [42]. It is proposed to test the ability of a scheme for capturing strong waves. The initial data

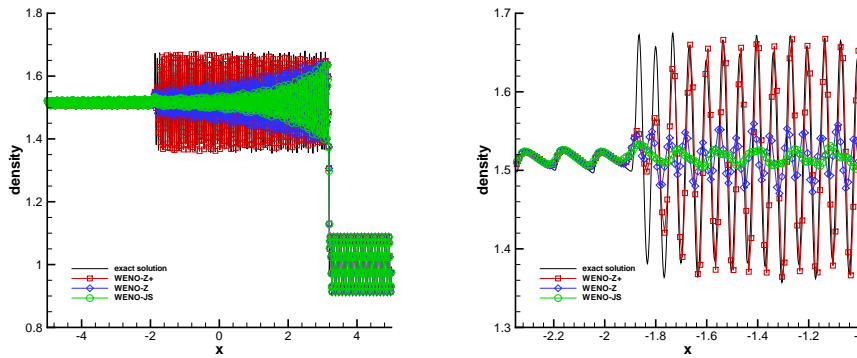$$(\rho, U, p) = \begin{cases} (10000, \ 0, \ 10000), & x < 0.3, \\ (1, \ 0, \ 1), & 0.3 < x. \end{cases}$$

Figure 1: The density distribution and local enlargement of Titarev-Toro problem with WENO-JS, WENO-Z and WENO-Z+ weights at $t = 5$, where $\lambda = \Delta x^{3/4}$ in WENO-Z+ methods.
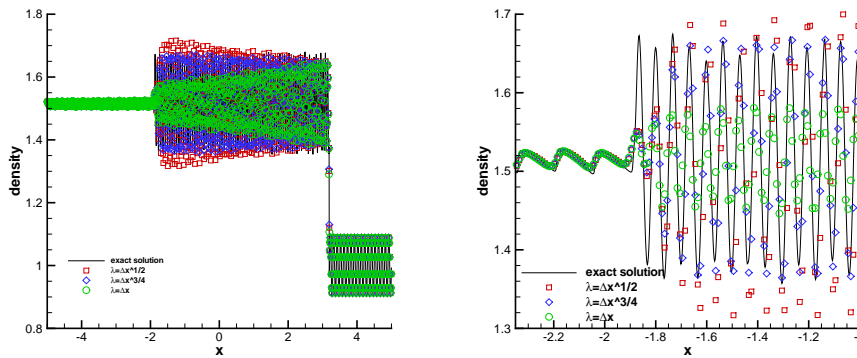

Figure 2: The density distribution and local enlargement of Titarev-Toro problem at $t = 5$ for WENO-Z+ weights with $\lambda = \Delta x^{1/2}$, $\Delta x^{3/4}$ and Δx.

The computational domain is $[0, 1]$ and the non-reflective boundary condition is used at both ends. It is a Sod-type problem, and the solution consists of a very strong rarefaction wave with the density variation from 10000 to 100, a contact discontinuity jumping from 100 to 8, and a shock wave jumping from 1 to 8. If uniform grid points are used, the density jump among neighboring cells inside the rarefaction wave is about 100 times the density jump in the shock layer. Hence the strong rarefaction wave is in a highly non-equilibrium state. It has been verified in [42] that many high order numerical methods have to use a very refined grid points in order to capture the rarefaction wave, the location of the shock, and the contact discontinuity properly. In this case, we start with the exact solution at time $t = 1.2$ as initial data, and the output time for the solution is $t = 12$, where both 100 and 200 uniform mesh points are used. The density and velocity distributions are shown in Fig. 3. If we start with the initial data at $t = 0$, i.e., a single jump at $x = 0.3$, the numerical solutions will not be as accurate as the above ones with the same grid points, although they are still acceptable. However, as the rarefaction wave is not so strong, the scheme works well, which is verified through another example with the density and pressure jumps from
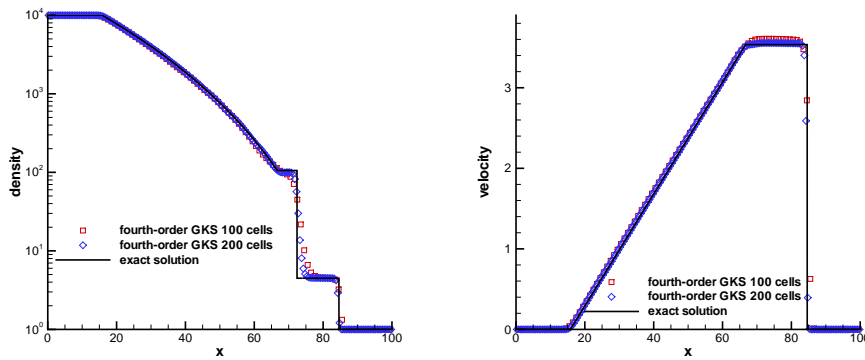
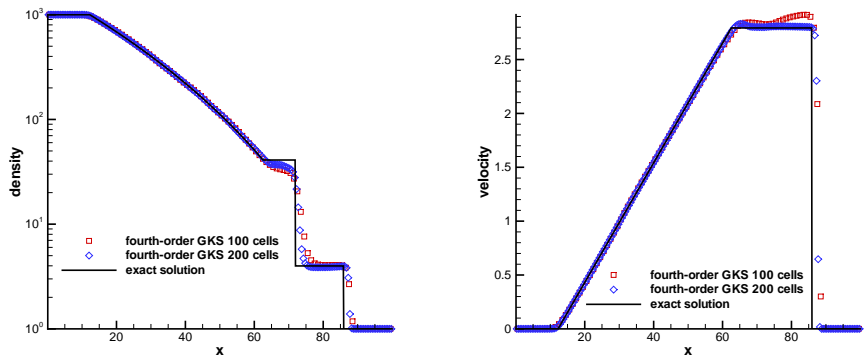Figure 3: Large density ratio problem with density variation from 10000 to 1 starting from $t = 1.2$.

Figure 4: Large density ratio problem with density variation from 1000 to 1 starting from $t = 0$.

10000 to 1000. The density and velocity distributions are shown in Fig. 4. The GRP simulation works better for such a case because the exact GRP solver is used for the Euler equations [26], especially at the initial time for the solution starting from a singular jump. This example shows that the flux is extremely important in capturing strong expansion waves.

3.2. Two-dimensional Riemann problems

In this subsection, five groups of two-dimensional benchmark problems are presented.

3.2.1. Hurricane-like solutions

The first group of two-dimensional time-dependent solution is the hurricane-like flow evolution, whose solution has one-point vacuum in the center with rotational velocity field. The initial condition is given as

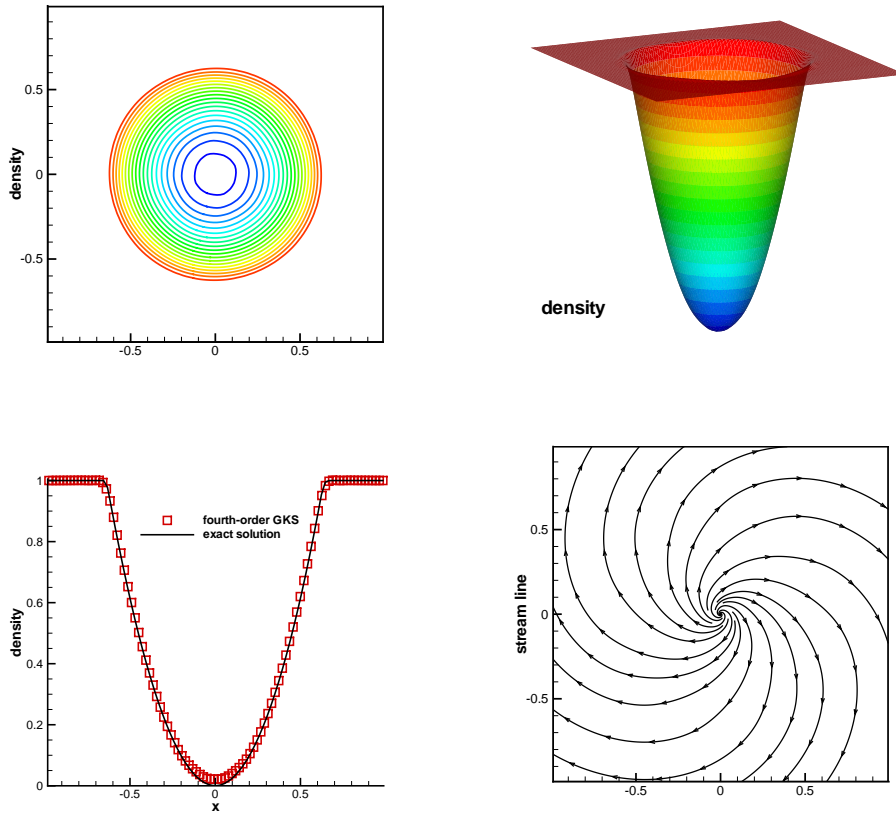$$(\rho, U, V, p) = (\rho_0, v_0 \sin \theta, -v_0 \cos \theta, A\rho_0^{\gamma}),$$

Figure 5: Hurricane-like solution: the critical case.

where $\theta = \arctan(y/x)$, A is the initial entropy, $\gamma = 2$. In this case, the initial velocity distribution has a nontrivial transversal component, which makes the flow rotational. The solutions are classified into three types [48] according to the initial Mach number $M_0 = |v_0|/c_0$, where c_0 is the sound speed.

1. Critical rotation with $M_0 = \sqrt{2}$. For this case, we have an exact solution with explicit formula. This solution consists of two parts: a far field solution and a near-field solution. The former far field solution is defined for $r \geq 2t\sqrt{p'(\rho_0)}$, $r = \sqrt{x^2 + y^2}$,

$$\begin{cases} U(x,y,t) = (2tp_0' \cos\theta + \sqrt{2p_0'}\sqrt{r^2 - 2t^2 p_0'} \sin\theta)/r, \\ V(x,y,t) = (2tp_0' \sin\theta - \sqrt{2p_0'}\sqrt{r^2 - 2t^2 p_0'} \cos\theta)/r, \\ \rho(x,y,t) = \rho_0, \end{cases} \tag{3.2}$$

and the near-field solution is defined for $r < 2t\sqrt{p'(\rho_0)}$

$$U(x,y,t) = \frac{x+y}{2t}, \quad V(x,y,t) = \frac{-x+y}{2t}, \quad \rho(x,y,t) = \frac{r^2}{8At^2}.$$

The curl of the velocity in the near-field is

$$curl(U,V) = V_x - U_y = -\frac{1}{2t} \neq 0,$$

and the solution has one-point vacuum at the origin $r = 0$. This is a typical hurricane-like solution that behaves highly singular, particularly near the origin $r = 0$.

There are two issues here challenging the numerical schemes: one is the presence of the vacuum state which examines whether a high order scheme can keep the positivity preserving property; the other is the rotational velocity field for testing whether a numerical scheme can preserve the symmetry. In our computation we take the data $A = 25$, $v_0 = 10$, $\rho_0 = 1$. The computational domain is $[-1,1] \times [-1,1]$, and the mesh size is $\Delta x = \Delta y = 1/100$. The boundary condition is given by the far field solution Eq. (3.2). Numerical results are presented in Fig. 5 at $t = 0.045$ with the distribution of density and velocity field. The positivity and symmetry are preserved well in the current scheme.

2. High-speed rotation with $M_0 > \sqrt{2}$. For this case, the density goes faster to the vacuum and the fluid rotates severely. In the computation $A = 25$, $v_0 = 12.5$, $\rho_0 = 1$. For this case, no exact solution can be imposed on the boundary. In the computation, the computational domain is $[-2,2] \times [-2,2]$, the mesh size is $\Delta x = \Delta y = 1/100$. Non-reflection boundary is given on the boundaries. The results in the domain $[-1,1] \times [-1,1]$, which is not affected by the boundary condition, is given in Fig. 6 at $t = 0.045$. Because of its high rotating speed, this case is more tough than the first one, and it can be used to validate the robustness of higher-order schemes.

3. Low-speed rotation with $M_0 < \sqrt{2}$. This case is milder than the other cases above. There is no vacuum in the solution, but it is still rotational with a low speed. In the computation $A = 25$, $v_0 = 7.5$, $\rho_0 = 1$. Similarly, the non-reflection boundary is given on the boundaries. The results in the domain $[-1,1] \times [-1,1]$ is presented in Fig. 6 at $t = 0.045$. The symmetry of the flow structure needs to be preserved.

3.2.2. Large Mach number limit

The second group is about the interactions of planar contact discontinuities, whose solutions in the large Mach number limit are singular and contain either vacuum or singular shocks or delta-shocks [27,28]. Two typical cases related to the large Mach number limit are provided in this group. As is well-known, the compressible fluid flows become incompressible at the low Mach number limit [33]. On the other hand, the large Mach number limit leads to the pressureless model [19,28]

$$\frac{\partial}{\partial t} \begin{pmatrix} \rho \\ \rho U \\ \rho V \\ \rho E \end{pmatrix} + \frac{\partial}{\partial x} \begin{pmatrix} \rho U \\ \rho U^2 \\ \rho UV \\ \rho EU \end{pmatrix} + \frac{\partial}{\partial y} \begin{pmatrix} \rho V \\ \rho UV \\ \rho V^2 \\ \rho EV \end{pmatrix} = 0. \tag{3.3}$$

This system can be also regarded as the zero moment closure of the Boltzmann-type equations [36] to describe the single transport effect of mass, momentum. The last equation
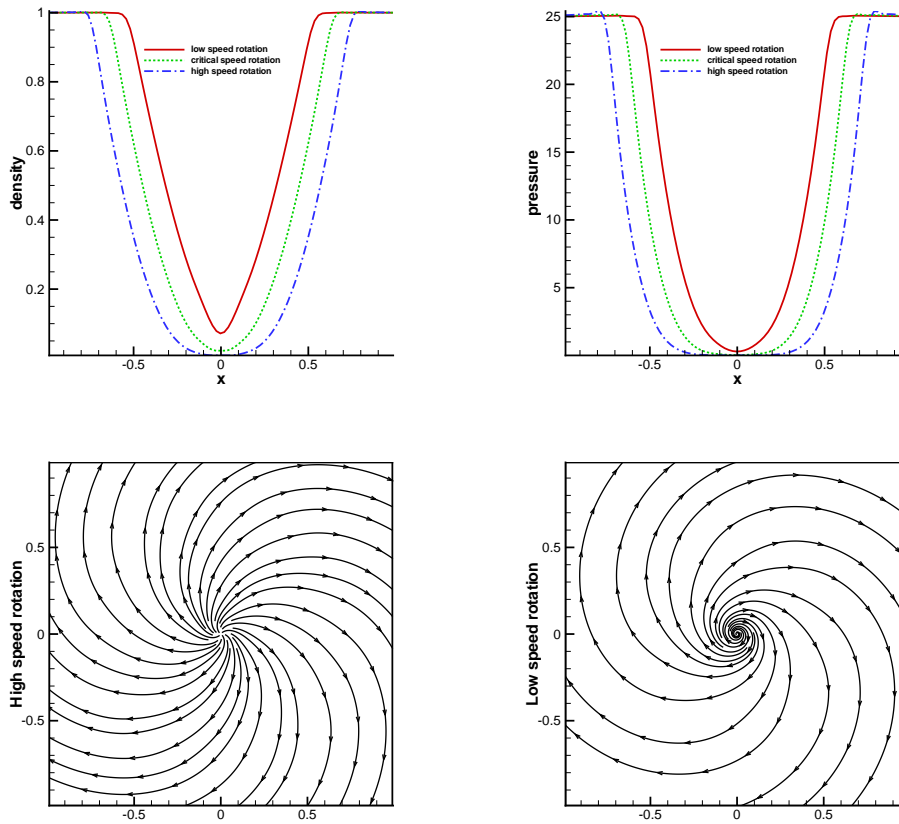
Figure 6: Hurricane-like solution: the cases of high speed rotation and low speed rotation.

in Eq. (3.3) is decoupled from the first three equations, and it is sufficient to consider the solution (ρ, U, V) of the first three equations of Eq. (3.3) in the limiting case.

The Riemann-type initial conditions for Eq. (3.1) are given as follows

$$(\rho, U, V, p) = \begin{cases} (\rho_1, U_1, V_1, p_1), & x > 0.5, \ y > 0.5, \\ (\rho_2, U_2, V_2, p_2), & x < 0.5, \ y > 0.5, \\ (\rho_3, U_3, V_3, p_3), & x < 0.5, \ y < 0.5, \\ (\rho_4, U_4, V_4, p_4), & x > 0.5, \ y < 0.5. \end{cases} \tag{3.4}$$

The negative contact discontinuity and positive contact discontinuity, which connect the l and r areas, are denoted as J_{lr}^- and J_{lr}^+ respectively

$$J_{lr}^- : w_l = w_r, \quad p_l = p_r, \quad w_l' \geq w_r',$$
$$J_{lr}^+ : w_l = w_r, \quad p_l = p_r, \quad w_l' \leq w_r'.$$

where w_l, w_r are the normal velocity and w_l', w_r' are the tangential velocity. Two types of interaction of planar contact discontinuities are considered as follows.
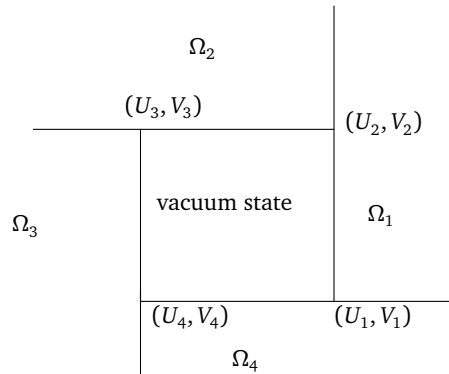
Figure 7: The solution of the pressureless equations Eq. (3.3) with the data (3.6). This figure is displayed in the self-similarity $(x/t, y/t)$–plane. The notation (U_i, V_i) denotes the coordinate $(x/t, y/t) = (U_i, V_i)$, $i = 1, 2, 3, 4$.
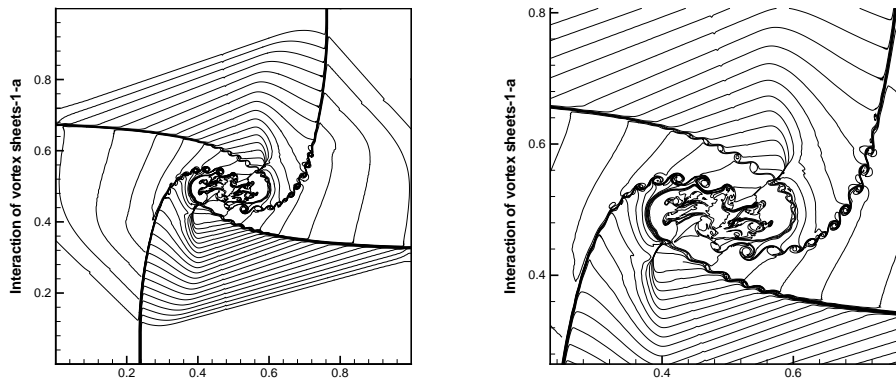

Figure 8: Density distribution and the local enlargement for the interaction of vortex sheets with same signs, where $p_0 = 1$.

1. Interaction of planar contact discontinuity for vortex sheets with same signs $J_{12}^- J_{32}^- J_{41}^- J_{34}^-$. The vacuum solutions will be provided by the large Mach number limit $[27, 40]$. For such a case, the initial data satisfies

$$U_1 = U_2 > U_3 = U_4, \qquad V_2 = V_3 > V_1 = V_4, \tag{3.5}$$

and in the computation, the initial data takes

$$\begin{cases} (\rho_1, U_1, V_1, p_1) = (1, -0.75, -0.5, p_0), \\ (\rho_2, U_2, V_2, p_2) = (2, -0.75, 0.5, p_0), \\ (\rho_3, U_3, V_3, p_3) = (1, 0.75, 0.5, p_0), \\ (\rho_4, U_4, V_4, p_4) = (3, 0.75, -0.5, p_0). \end{cases} \tag{3.6}$$

This initial pressure distribution p_0 is uniform and the density distribution could be arbitrary. Four planar contact discontinuities J_{ij}^- separate neighboring states and support the
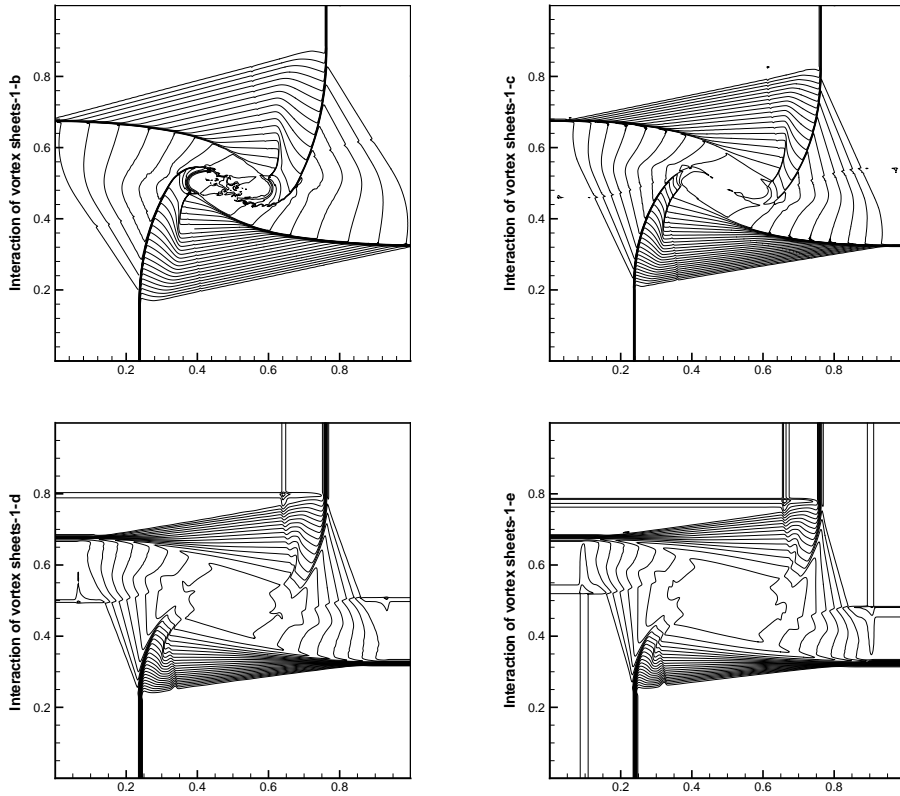
Figure 9: Density distributions for the interaction of vortex sheets with same signs, where $p_0 = 0.5, 0.25, 0.15$ and 0.1.

same sign vortex sheets. On the contact discontinuity J_{21}^-, the density undergoes a jump, and the vorticity is a singular measure

$$curl(U, V) = (V_1 - V_2)\delta(x - U_1 t, y, t), \quad V_1 - V_2 < 0,$$

where $\delta(x, y, t)$ is the standard Dirac function (measure). Therefore, this contact discontinuity is the composite of an entropy wave and a vortex sheet. The same applies for J_{23}^-, J_{34}^-, and J_{41}^-. Their instantaneous interaction results in a complex wave pattern. The limiting system Eq. (3.3) has an explicit formula that consists of four constant states in $\Omega_i, i = 1, 2, 3, 4$, and a vacuum state inside a pyramid with edges $(x/t, y/t) = (U_i, V_i)$, i.e.

$$(\rho, U, V, p)(x, y, t) = \begin{cases} (\rho_i, U_i, V_i, p_0), & (x, y, t) \in \Omega_i, \\ \text{vacuum}, & (x, y, t) \text{ in the pyramid}. \end{cases}$$

The solution is schematically described in Fig. 7.

We use the fourth order gas-kinetic scheme to look into the asymptotic process for this problem by setting the pressure smaller and smaller. The initial pressure is taken to be $p_0 = 1, 0.5, 0.25, 0.15$, and 0.1, respectively. The computation domain is $[0, 1] \times [0, 1]$ and the
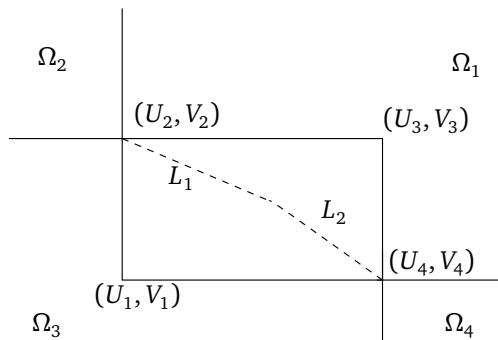
Figure 10: The delta-shock solution of the pressureless equations due to the interaction of vortex sheets. This figure is displayed in the self-similarity $(x/t, y/t)$–plane. The notation (U_i, V_i) denotes the coordinate $(x/t, y/t) = (U_i, V_i)$, $i = 1, 2, 3, 4$. The dashed line denotes the support of delta-shocks.
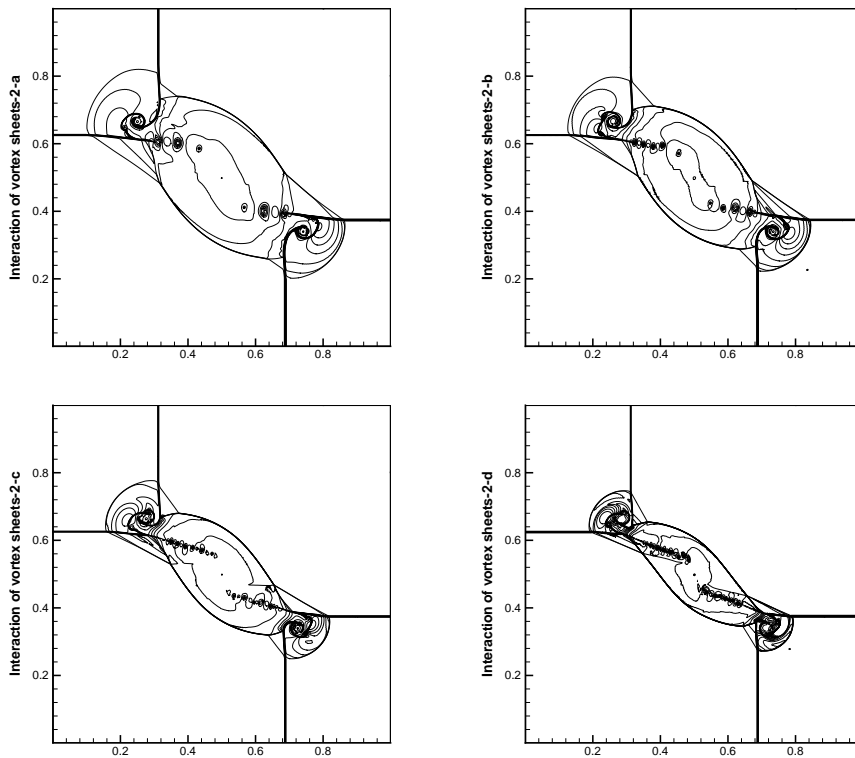

Figure 11: Density distributions for the interaction of vortex sheets with different signs, with $p_0 = 1, 0.75, 0.5$ and 0.3.

non-reflection condition is used for the boundaries. The density distributions are displayed in Fig. 8 and Fig. 9 at $t = 0.35$. The uniform mesh with $\Delta x = \Delta y = 1/1500$ is used for $p_0 = 1, 0.5$, and 0.25. It is observed that as $p_0 = 1$ (the Mach number M_0 is relatively large), the numerical solution displays more small scale structures. With the increase of
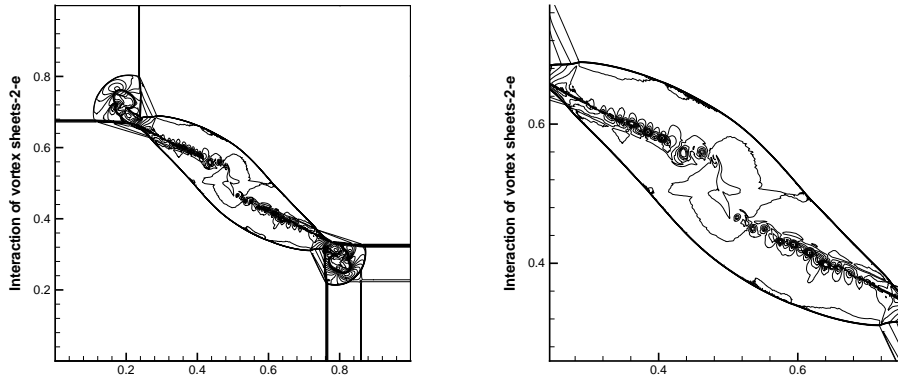
Figure 12: Density distribution and the local enlargement for the interaction of vortex sheets with different signs, with $p_0 = 0.2$.

the initial Mach number M_0, the complicated flow structure disappears. Uniform mesh with $\Delta x = \Delta y = 1/400$ is used for the cases with $p_0 = 0.15$, 0.1. The solution becomes much closer to that given in Fig. 7 in the limiting low pressure case.

2. Interaction of planar contact discontinuities for vortex sheets with different signs $J_{21}^- J_{32}^+ J_{41}^+ J_{34}^-$. For such a case, the delta-shock solutions will be emerged in the large Mach number limit [27, 40]. The initial data is designed so as to satisfy

$$U_3 = U_4 > U_1 = U_2, \qquad V_2 = V_3 > V_1 = V_4.$$

The initial pressure distribution is also uniform and the density distribution is arbitrary. This case is different from the first case in this group. The four planar contact discontinuities support vortex sheets of different signs and their interactions produce totally different flow patterns. With such initial data, the solution of Eq. (3.3) has a singular solution containing so-called delta-shocks, as shown in Fig. 10. The solution formula is

$$(\rho, U, V)(x, y, t) = (\rho_i, U_i, V_i), \quad (x, y, t) \in \Omega_i. \tag{3.7}$$

However, the solution becomes singular, particularly, the density takes a singular measure on the support $L_1 \cup L_2$ in Fig. 10

$$\rho(x, y, t) = \sqrt{\rho_1 \rho_3}\, \delta(x - x(t, s), y - y(t, s), t), \tag{3.8}$$

where

$$(x, y) = (x(t, s), y(t, s))$$

represents the support $L_1 \cup L_2$ of the Dirac measure in Fig. 10.

The numerical simulations are designed for the cases of different Mach numbers. The

initial condition is given as follows

$$
\begin{cases}
(\rho_1, U_1, V_1, p_1) = (1, 0.75, -0.5, p_0), \\
(\rho_2, U_2, V_2, p_2) = (2, 0.75, 0.5, p_0), \\
(\rho_3, U_3, V_3, p_3) = (1, -0.75, 0.5, p_0), \\
(\rho_4, U_4, V_4, p_4) = (3, -0.75, -0.5, p_0).
\end{cases}
$$

The uniform mesh with $\Delta x = \Delta y = 1/1500$ is used. The computation domain is $[0,1] \times [0,1]$ and the non-reflection condition is used for the boundaries. The density distributions are presented in Fig. 11 for the cases with initial pressure $p_0 = 1$, 0.75, 0.5, and 0.3 respectively, at the output time $t = 0.25$. With the decrease of the pressure, or equivalently with the increase of initial Mach number, it is observed that more and more small scaled vortices are present in the solutions. For the case with $p_0 = 0.2$, the density distribution is presented in Fig. 12 at $t = 0.28$. The solution tends to be very close to the solution Eqs. (3.7)-(3.8). This benchmark test validates the capability of higher-order scheme to preserve the asymptotical stability for large Mach number flow simulations.

3.2.3. Transition from continuous flows to the present of shocks

This group is about the interaction of two-dimensional planar rarefaction waves, from which a continuous transition from smooth flow to the presence of transonic shock will emerge. A global continuous solution is constructed in [29] with a clear physical picture for the bi-symmetrical interaction only when the rarefaction waves involved are weak. In general, such a bi-symmetric interaction may result in the presence of shocks, which never occur in the one-dimensional case since the interaction of one-dimensional rarefaction waves produces only continuous solutions [11]. The backward rarefaction wave and forward rarefaction wave, which connect the l and r areas, are denoted as $\overleftarrow{R}_{lr}$ and $\overrightarrow{R}_{lr}$. The two cases with four planar rarefaction waves $\overrightarrow{R}_{21}\overleftarrow{R}_{32}\overrightarrow{R}_{41}\overleftarrow{R}_{34}$ have the following initial conditions,

$$
\begin{cases}
(\rho_1, U_1, V_1, p_1) = (1, 0.6233, 0.6233, 1.5), \\
(\rho_2, U_2, V_2, p_2) = (0.389, -0.6233, 0.6233, 0.4), \\
(\rho_3, U_3, V_3, p_3) = (1, -0.6233, -0.6233, 1.5), \\
(\rho_4, U_4, V_4, p_4) = (0.389, 0.6233, -0.6233, 0.4),
\end{cases}
\tag{3.9}
$$

and

$$
\begin{cases}
(\rho_1, U_1, V_1, p_1) = (1, 0.0312, 0.0312, 0.5), \\
(\rho_2, U_2, V_2, p_2) = (0.927, -0.0312, 0.0312, 0.45), \\
(\rho_3, U_3, V_3, p_3) = (1, -0.0312, -0.0312, 0.5), \\
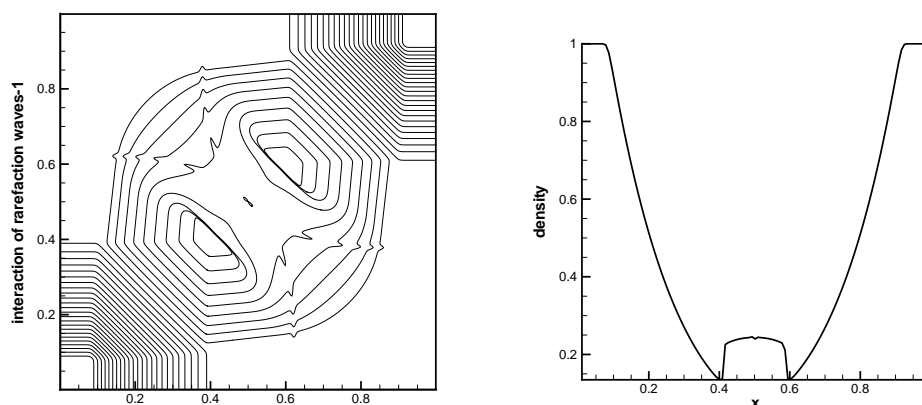(\rho_4, U_4, V_4, p_4) = (0.927, 0.0312, -0.0312, 0.45).
\end{cases}
\tag{3.10}
$$

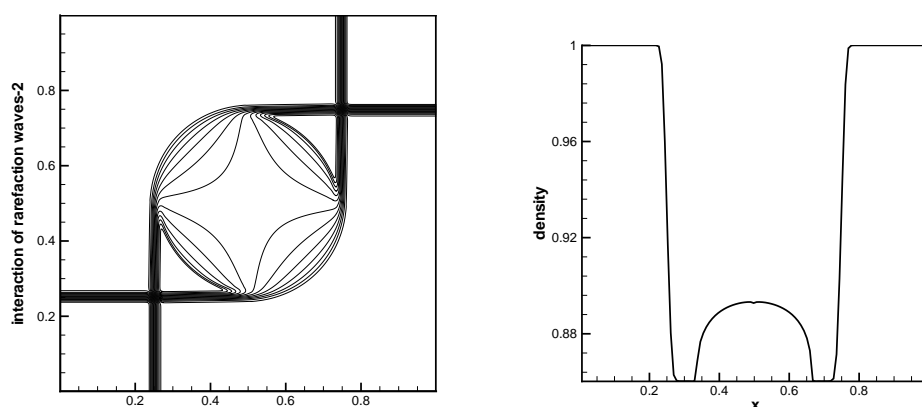Figure 13: Interaction of planar rarefaction waves with initial condition Eq.(3.9).

Figure 14: Interaction of planar rarefaction waves with initial condition Eq. (3.10).

The computation domain is $[0,1] \times [0,1]$ and the non-reflection condition is used for the boundaries. The numerical results are presented in Figs. 13-14, in which a uniform mesh with $\Delta x = \Delta y = 1/400$ is used. For the solution with the initial condition Eq. (3.9), the planar rarefaction waves are strong and shocks are present in the interior domain, for which there was a thorough study on the criterion for the shock formation [15]. On the contrary, if the planar rarefaction waves are relatively weak, e.g., with the initial data Eq. (3.10), the global solution is continuous [29], but the density in the interior domain is quite low, as shown in Fig. 14. So the interaction of planar rarefaction waves in the current benchmark tests is associated with multiple scale nature and the numerical results in Figs. 13-14 are fully consistent with the theoretical analysis in [15, 29].

3.2.4. Multiscale wave structures resulting from shock wave interactions

The fourth group deals with the interaction of shocks, and tests the ability of higher-order schemes in the capturing of solutions with small scale structure. The study of shock wave

interactions is always one of central topics in gas dynamics and related fields. The benchmark problems of step-facing shock interaction and the oblique shock reflection presented in [45] were proposed in early 80s, which have been used for almost all newly designed schemes afterwards. This can be seen from the huge number of the Google citations to the original paper. The two-dimensional Riemann problems [49] with four planar shocks $\overleftarrow{S}_{21}\overleftarrow{S}_{32}\overleftarrow{S}_{41}\overleftarrow{S}_{34}$ have been tested, where the backward rarefaction wave and forward rarefaction wave connecting the l and r areas are denoted as $\overleftarrow{S}_{lr}$ and $\overrightarrow{S}_{lr}$. To obtain the detailed flow structure with less computational mesh points, the initial condition are given as follows

$$
\begin{cases}
(\rho_1, U_1, V_1, p_1) = (1.5, 0, 0, 1.5), & x > 0.8, \ \ y > 0.8, \\
(\rho_2, U_2, V_2, p_2) = (0.5323, 1.206, 0, 0.3), & x < 0.8, \ \ y > 0.8, \\
(\rho_3, U_3, V_3, p_3) = (0.138, 1.206, 1.206, 0.029), & x < 0.8, \ \ y < 0.8, \\
(\rho_4, U_4, V_4, p_4) = (0.5323, 0, 1.206, 0.3), & x > 0.8, \ \ y < 0.8.
\end{cases}
\tag{3.11}
$$

The computation domain is $[0,1] \times [0,1]$ and the non-reflection condition is used for the boundaries. The numerical solution is displayed in Fig. 15, where a uniform mesh with $\Delta x = \Delta y = 1/1000$ is used. This case is just the mathematical formation of the reflection problem of oblique shocks in [45] and the symmetric line $x = y$ can be regarded as the rigid wall. Such a formulation can avoid the complexity of numerical boundary conditions and make the simulation simple. Any higher-order numerical scheme can test it easily without involving numerical treatment of boundary conditions. The gas-kinetic schemes with second-order and fourth-order temporal accuracy are tested with the same fifth-order WENO initial spatial data reconstruction at each time level. Based on the simulation results, it is obvious that the second order scheme is much more dissipative than the fourth-order one. The small scaled vortices are resolved sharply using the fourth-order GKS. To capture the small scale structure is important for the simulation of turbulent flows, which present complex flow structure experimentally [23–25].

3.3. Conservation laws with source terms

The last group is the Rayleigh-Taylor instability to test the performance of higher-order scheme for the conservation laws with source terms, and the governing equations are written as

$$
\frac{\partial}{\partial t}
\begin{pmatrix} \rho \\ \rho U \\ \rho V \\ \rho E \end{pmatrix}
+ \frac{\partial}{\partial x}
\begin{pmatrix} \rho U \\ \rho U^2 + p \\ \rho UV \\ U(\rho E + p) \end{pmatrix}
+ \frac{\partial}{\partial y}
\begin{pmatrix} \rho V \\ \rho UV \\ \rho V^2 + p \\ V(\rho E + p) \end{pmatrix}
=
\begin{pmatrix} 0 \\ 0 \\ \rho \\ \rho V \end{pmatrix}.
$$

The Rayleigh-Taylor instability happens on the interface between fluids with different densities when an acceleration is directed from the heavy fluid to the light one. The instability with fingering nature generates bubbles of light fluid rising into the ambient heavy fluid
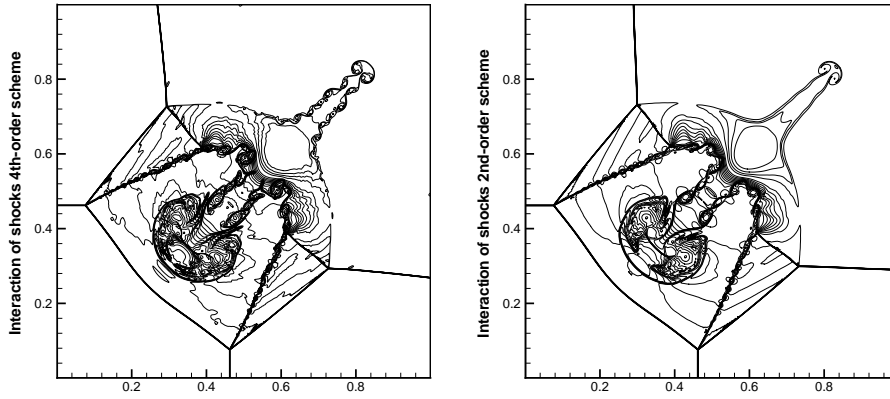
Figure 15: The density distribution for the fourth-order scheme and second-order scheme with $\Delta x = \Delta y = 1/1000$ for the shock wave interactions.
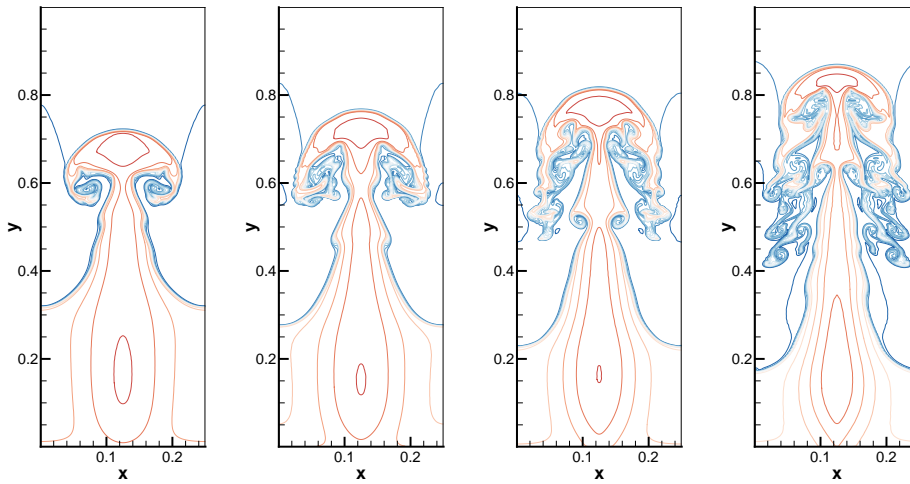

Figure 16: Rayleigh-Taylor instability: density distribution with the mesh size $\Delta x = \Delta y = 1/800$ at $t = 1.75, 2, 2.25$ and 2.5.

and spikes of heavy fluid falling into the light fluid. The initial condition of this problem [39] is given as follows

$$
\begin{cases}
(\rho, U, V, p) = \big(2,\ 0,\ -0.025c\cos(8\pi x, 2y+1)\big), & x \le 0.5, \\
(\rho, U, V, p) = \big(1,\ 0,\ -0.025c\cos(8\pi x, y+3/2)\big), & x > 0.5,
\end{cases}
$$

where $c = \sqrt{\gamma p/\rho}$ is the sound speed and $\gamma = 5/3$. The computational domain is $[0, 0.25] \times [0, 1]$. The reflecting boundary conditions are imposed for the left and right boundaries. At the top boundary, the flow variables are set as $(\rho, U, V, p) = (1, 0, 0, 2.5)$. At the bottom boundary, they are $(\rho, U, V, p) = (2, 0, 0, 1)$. The source terms $S(\mathbf{w})$ is given by the cell averaged value $\mathbf{w}$ and $\partial_t S(\mathbf{w}) = (0, 0, \partial_t \rho, \partial_t(\rho V))$ is given by the governing
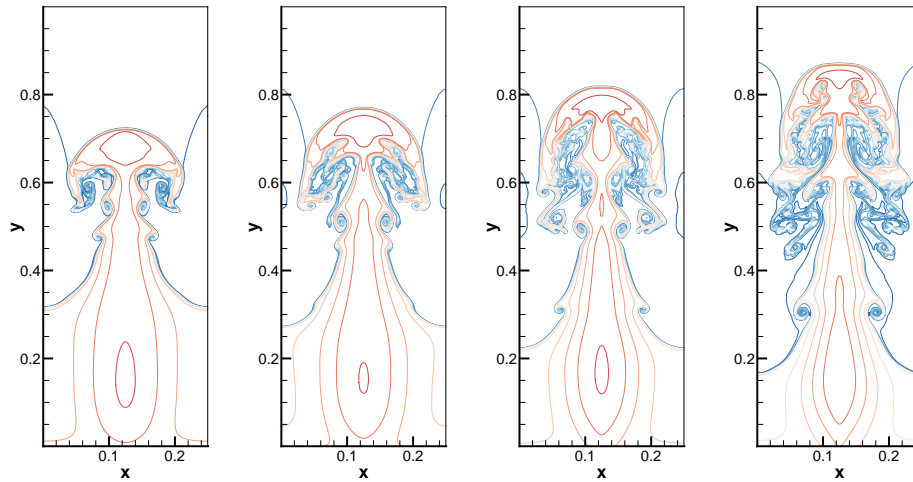
Figure 17: Rayleigh–Taylor instability: density distribution with the mesh size $\Delta x = \Delta y = 1/1600$ at $t = 1.75, 2, 2.25$ and 2.5.

equation, respectively. The uniform meshes with $\Delta x = \Delta y = 1/800$ and $1/1600$ are used in the computation. The density distributions at $t = 1.75, 2, 2.25$, and 2.5 are presented in Fig. 16 and Fig. 17. With the mesh refinement, the complicated flow structures are observed. It is a test to check the suitability of higher-order schemes for the capturing of interface instabilities.

4. Conclusions

In the past decades, gigantic amount of higher-order schemes for the compressible Euler equations have been proposed, and they all have excellent performance in the traditional test cases designed thirty years ago for validating the performance of mainly second-order schemes [45]. These old test cases can hardly distinguish the performance of the current higher-order schemes. In order to set up a new standard to guide the further development of higher-order schemes, in this paper a few benchmark cases are suggested. The construction of accurate and robust higher-order schemes for the Euler equations is related to many numerical and physical modeling issues. At current stage, in terms of flow dynamics the design of higher-order schemes is still based on the exact Riemann solution or any other simplified approximate Riemann solvers. The focus of the higher-order approaches under the frameworks of DG, finite difference, and finite volume, concentrates mostly on the underlying data reconstruction or limiters. The necessity of higher-order dynamics, such as the close coupling of temporal-spatial flow evolution in the flux function, has not been considered with sufficient attention. This may be one of the reasons for the stagnation on the development of higher-order schemes in recent years. For higher-order schemes, the improvement of time accuracy in the flux modeling may become important for the improvement of the robustness and accuracy of the schemes, and for the capturing of multiple scale flow structure with complicated wave interactions. Most benchmark tests

in this paper are for the time accurate flow evolutions, which are closely related to the hyperbolic nature of the Euler equations. These test cases impose a new level of quality control on the higher-order schemes. To get good performance on all these cases requires the construction of higher-order schemes on a more physically and mathematically consistent way than the current existing high-order methodology.

References

[1] R. Borges, M. Carmona, B. Costa and W. S. Don, *An improved weighted essentially non-oscillatory scheme for hyperbolic conservation laws*, J. Comput. Phys., 227 (2008), pp. 3191–3211.

[2] F. Acker, R. B. De R. Borges and B. Costa, *An improved WENO-Z scheme*, J. Comput. Phys., 313 (2016), pp. 726–753.

[3] M. Ben-Artzi, J. Falcovitz, *A second-order Godunov-type scheme for compressible uid dynamics*, J. Comput. Phys., 55 (1984), pp. 1–32.

[4] M. Ben-Artzi, J. Li and G. Warnecke, *A direct Eulerian GRP scheme for compressible fluid flows*, J. Comput. Phys., 218 (2006), pp. 19–43.

[5] M. Ben-Artzi and J. Li, *Hyperbolic conservation laws: Riemann invariants and the generalized Riemann problem*, Numerische Mathematik, 106 (2007), pp. 369–425.

[6] P. L. Bhatnagar, E. P. Gross and M. Krook, *A Model for Collision Processes in Gases I: Small Amplitude Processes in Charged and Neutral One-Component Systems*, Phys. Rev., 94 (1954), pp. 511–525.

[7] J. P. Boris, *A fluid transport algorithm that works, in: Computing as a Language of Physics*, International Atomic Energy Commision, (1971), pp. 171–189.

[8] S. Chapman and T. G. Cowling, The Mathematical Theory of Non-Uniform Gases, 3rd ed, Cambridge University Press, (1990).

[9] A. J. Christlieb, S. Gottlieb, Z. Grant and D. C. Seal, *Explicit strong stability preserving multistage two-derivative time-stepping scheme*, J. Sci. Comp., 68 (2016), pp. 914–942.

[10] B. Cockburn and C. W. Shu, *TVB Runge-Kutta local projection discontinuous Galerkin finite element method for conservation laws II: general framework*, Math. Comput., 52 (1989), pp. 411–435.

[11] R. Courant and K. O. Friedrichs, Supersonic Flow and Shock Waves, Springer, (1948).

[12] B. Cockburn and C. W. Shu, *The Runge-Kutta discontinuous Galerkin method for conservation laws V: multidimensional systems*, J. Comput. Phys., 141 (1998), pp. 199–224.

[13] A. Harten, *High resolution schemes for hyperbolic conservation laws*, J. Comput. Phys., 49 (1983), pp. 357–393.

[14] E. Han, J. Li and H. Tang, *Accuracy of the adaptive GRP scheme and the simulation of 2-D Riemann problem for compressible Euler equations*, Comm. Comput. Phys., 10 (2011), pp. 577-606.

[15] J. Glimm, X. Ji, J. Li, X. Li, P. Zhang, T. Zhang and Y. Zheng, *Transonic shock formation in a rarefaction Riemann problem for the 2D compressible Euler equations*, SIAM J. Appl. Math., 69 (2008), pp. 720–742.

[16] A. HARTEN, B. ENGQUIST, S. OSHER AND S. R. CHAKRAVARTHY, *Uniformly high order accurate essentially non-oscillatory schemes*, III. J. Comput. Phys., 71 (1987), pp. 231–303.

[17] G. S. JIANG AND C. W. SHU, *Efficient implementation of Weighted ENO schemes*, J. Comput. Phys., 126 (1996), pp 202–228.

[18] V. P. KOLGAN, *Application of the principle of minimum values of the derivative to the construction of finite-difference schemes for calculating discontinuous solutions of gas dynamics*, Scientific Notes of TsAGI, 3 (1972), pp. 68–77.

[19] H. O. KREISS AND J. LORENZ, Initial-Boundary Value Problems and the Navier-Stokes Equations, Academic Press, (2004).

[20] *A. Kurganov and E. Tadmor*, Solution of two-dimensional Riemann problems for gas dynamics without Riemann problem solvers, Numer. Meth. Part. Diff. Eqs., 18 (2002), pp. 584–608.

[21] P. D. LAX AND X. D. LIU, *Solution of two-dimensional Riemann problems of gas dynamics by positive schemes*, SIAM J. Sci. Comput., 19 (1998), pp. 319–340.

[22] P. LAX AND B. WENDROFF, *Systems of conservation laws*, Comm. Pure Appl. Math., 13 (1960), pp. 217–237.

[23] C. B. LEE, *New features of CS solitons and the formation of vortices*, Phys. Lett. A, 247(6) (2008), pp. 397–402.

[24] C. B. LEE, *Possible universal transitional scenario in a flat plate boundary layer: Measurement and visualization*, Phys. Rev. E, 62(3) (2000), 3659.

[25] C. B. LEE AND J. Z. WU, *Transition in wall-bounded flows*, Appl. Mech. Rev., 61(3) (2008), 0802.

[26] J. LI, Z. DU, A Two-Stage Fourth Order Time-Accurate Discretization for Lax-Wendroff Type Flow Solvers, I. Hyperbolic Conservation Laws, Mathematics, 2016.

[27] J. LI, T. ZHANG AND S. YANG, The Two-Dimensional Riemann Problem in Gas Dynamics, Addison Wesley Longman, (1998).

[28] J. LI, *Note on the compressible Euler equations with zero temperature*, Appl. Math. Lett., 14 (2001), pp. 519–523.

[29] J. LI AND Y. ZHENG, *Interaction of four rarefaction waves in the bi-symmetric class of the two-dimensional Euler equations*, Comm. Math. Phys., 296 (2010), pp. 303–321.

[30] Q. LI, K. XU AND S. FU, *A high-order gas-kinetic Navier-Stokes flow solver*, J. Comput. Phys., 229 (2010), pp. 6715–6731.

[31] X. D. LIU, S. OSHER AND T. CHAN, *Weighted essentially non-oscillatory schemes*, J. Comput. Phys., 115 (1994), pp. 200–212.

[32] J. LUO AND K. XU, *A high-order multidimensional gas-kinetic scheme for hydrodynamic equations*, Science China Technological Sciences, 56 (2013), pp. 2370–2384.

[33] A. MAJDA, Compressible Fluid Flow and Systems of Conservation Laws in Several Space Variables, Applied Mathematical Sciences, Springer-Verlag, New York, 53 (1984).

[34] L. PAN, K. XU, Q. LI AND J. LI, *An efficient and accurate two-stage fourth-order gas-kinetic scheme for the Navier-Stokes equations*, J. Comput. Phys. 326 (2016), pp. 197–221.

[35] W. H. REED AND T. R. HILL, Triangular Mesh Methods for the Neutron Transport Equation, Technical Report LA-UR-73-479, Los Alamos Scientific Laboratory, Los Alamos, 1973.

[36] W. E, Y. G. RYKOV AND Y. G. SINAI, *Generalized variational principles, global weak solutions and behavior with random initial data for systems of conservation laws arising in adhesion particle dynamics*, Comm. Math. Phys., 177 (1996), pp. 349–380.

[37] C. W. SCHULZ-RINNE, J. P. COLLINS AND H. M. GLAZ, *Numerical solution of the Riemann problem for twodimensional gas dynamics*, SIAM J. Sci. Comput., 14 (1993), pp. 1394–1414.

[38] D. C. SEAL, Y. GÜCLÜ AND A. J. CHRISTLIEB, *High-order multiderivative time integrators for hyperbolic conservation laws*, J. Sci. Comp., 60 (2014), pp. 101–140.

[39] J. Shi, Y. T. Zhang and C. W. Shu, *Resolution of high order WENO schemes for complicated flow structures*, J. Comput. Phys., 186 (2003), pp. 690–696.

[40] W. Sheng and T. Zhang, *The Riemann problem for the transportation equations in gas dynamics*, Mem. Amer. Math. Soc., 654(654) (1999), pp. 77.

[41] C. W. Shu and S. Osher, *Efficient implementation of essentially non-oscillatory shock capturing schemes*, J. Comput. Phys., 77 (1988), pp. 439–471.

[42] H. Z. Tang and T. G. Liu, *A note on the conservative schemes for the Euler equations*, J. Comput. Phys., 218 (2006), pp. 451–459.

[43] V. A. Titarev and E. F. Toro, *Finite volume WENO schemes for three-dimensional conservation laws*, J. Comput. Phys. 201 (2014), pp. 238–260.

[44] B. van Leer, *Towards the ultimate conservative difference scheme. V. A second order sequel to Godunov's method*, J. Comput. Phys., 32 (1979), pp. 101–136.

[45] P. Woodward and P. Colella, *Numerical simulations of two-dimensional fluid flow with strong shocks*, J. Comput. Phys., 54 (1984), pp. 115–173.

[46] K. Xu, *Direct modeling for computational fluid dynamics: construction and application of unfied gas kinetic schemes*, World Scientific, (2015).

[47] K. Xu, *A gas-kinetic BGK scheme for the Navier-Stokes equations and its connection with artificial dissipation and Godunov method*, J. Comput. Phys., 171 (2001), pp. 289–335.

[48] T. Zhang and Y. Zheng, *Exact spiral solutions of the two-dimensional Euler equations*, Discrete Contin. Dynam. Systems, 3 (1997), pp. 117–133.

[49] T. Zhang and Y. Zheng, *Conjecture on the structure of solutions of the Riemann problem for two dimensional gas dynamics systems*, SIAM J. Math. Anal., 21 (1990), pp. 593–630.